Computers in Biology and Medicine 182 (2024) 109154

Contents lists available at ScienceDirect

Computers in Biology and Medicine

journal homepage: www.elsevier.com/locate/compbiomed

MV-GNN: Generation of continuous geometric representations of mitral valve motion from 3D+t echocardiography

Matthias Ivantsits [a,b,*], Lennart Tautz [c], Markus Huellebrand [a,b,c], Lars Walczak [a,b,c], Serdar Akansel [b], Inna Khasyanova [b], Jörg Kempfert [b,d], Simon Sündermann [b,d], Volkmar Falk [b,d], Anja Hennemuth [a,b,c,d]

[a] Institute for Imaging Science and Computational Modelling in Cardiovascular Medicine, Charité – Universitätsmedizin Berlin, 13353 Berlin, Germany
[b] Deutsches Herzzentrum der Charité, 13353 Berlin, Germany
[c] Fraunhofer MEVIS, Max-von-Laue-Str. 2, 28359 Bremen, Germany
[d] DZHK (German Centre for Cardiovascular Research), Berlin, Germany

ARTICLE INFO

Keywords:
3D+t transesophageal echocardiography
Geometric deep learning
Graph network models
Mitral valve reconstruction

ABSTRACT

We present a geometric deep-learning method for reconstructing a temporally continuous mitral valve surface mesh from 3D transesophageal echocardiography sequences. Our approach features a supervised end-to-end deep learning architecture that combines a convolutional neural network-based voxel encoder and decoder with a graph neural network-based multi-resolution mesh decoder, all trained on sparse landmark annotations. Key elements of our methodology include a tube-shaped prototype mesh with labeled vertices, a specialized loss function to preserve the known inlet and outlet, and a rigid alignment system for anatomical landmarks. A custom term in the loss function prevents self-intersecting geometries within the valve mesh, promoting point correspondence and facilitating a continuous representation of valve anatomy over time. An ablation study evaluates the impact of different loss term configurations on model performance, highlighting the effectiveness of each individual loss term. Our Mitral Valve Graph Neural Network (MV-GNN) outperforms existing deep-learning methods on most distance metrics for the annulus and leaflets. The continuous valve motion representations generated by our approach (3D+t) exhibit distance measures comparable to our 3D solution, demonstrating its potential for analyzing mitral valve dynamics and enhancing personalized simulations for hemodynamic assessment and therapy planning.

1. Introduction

The mitral valve regulates blood flow between the heart's left atrium and ventricle. The valve apparatus consists of the anterior and posterior leaflets, which are divided by two distinct morphological indentations known as the commissures (see Fig. 1). During the diastolic phase, the valve opens to enable the filling of the left ventricle with oxygenated blood. The intraventricular pressure during heart muscle contraction triggers the mitral valve to close in the systolic phase to avoid regurgitation.

Fig. 2 shows typical mitral valve apparatus pathological alterations. In Type I pathologies [1], the mitral valve annulus is dilated, hindering full closure during systole. In Type II patients, chordae tendineae (chords from here on) connecting leaflets and papillary muscles are ruptured so that the loose part of the valve may protrude into the atrium during ventricle contraction, thereby hindering valve closure in systole. The gold-standard imaging method for diagnosis and treatment planning is 3D transesophageal echocardiography (TEE) [2,3]. 3D TEE sequences enable the inspection of mitral valve anatomy and motion. Automatic and semi-automatic algorithms for analyzing echocardiographic data have been evaluated with promising results for the assessment of diseases such as mitral valve regurgitation [4].

Abbreviations: 3D-time-sequence, (**3D+t**); Chordae tendineae, (**chords**); Convolutional neural network, (**CNN**); Deep-learning, (**DL**); Fully connected, (**FC**); Graph convolution + upsampling, (**GCU**); Graph neural network, (**GNN**); Latent space, (**LS**); Mitral valve graph neural network, (**MV-GNN**); Multiplanar reformation, (**MPR**); Neighborhood sampling, (**NHS**); Rigid registration, (**RR**); Transesophageal echocardiography, (**TEE**); Voxel convolution + upsampling, (**VCU**)

* Corresponding author at: Institute for Imaging Science and Computational Modelling in Cardiovascular Medicine, Charité – Universitätsmedizin Berlin, 13353 Berlin, Germany.
E-mail address: matthias.ivantsits@dhzc-charite.de (M. Ivantsits).

https://doi.org/10.1016/j.compbiomed.2024.109154
Received 26 February 2024; Received in revised form 17 August 2024; Accepted 11 September 2024
Available online 24 September 2024
0010-4825/© 2024 The Authors. Published by Elsevier Ltd. This is an open access article under the CC BY license (http://creativecommons.org/licenses/by/4.0/).

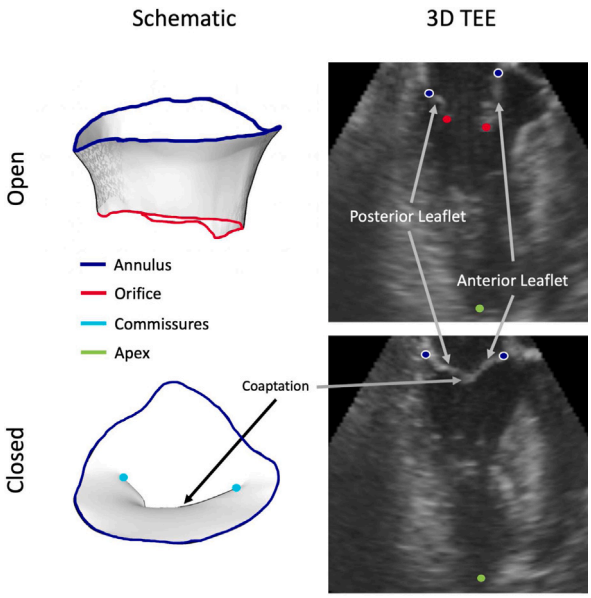

Fig. 1. Anatomical landmarks used by the proposed approach. On the left, the valve is visualized as a 3D surface in an open and closed state. On the right 3D TEE image slices centered on the mitral valve are shown. This illustration includes positions for the anterior and posterior leaflets, annulus, orifice, coaptation, commissures, and apex.

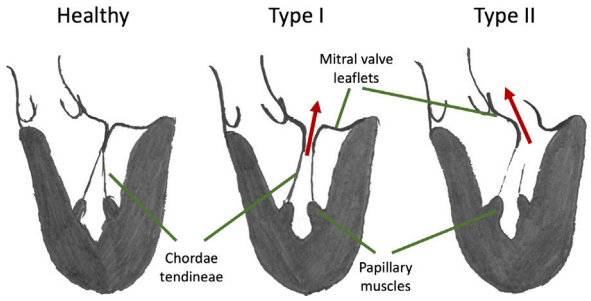

Fig. 2. Typical mitral valve apparatus pathological alterations. In Type I pathologies, the mitral valve annulus is dilated, hindering full closure during systole. In Type II pathologies, chords connecting leaflets and papillary muscles are ruptured. In this condition, the leaflet may regurgitate during systole.

Capturing the mitral valve anatomy in echocardiographic image data is challenging due to the fast-moving thin valve leaflets, which might be covered by only 1–2 voxels and blurred depending on the spatiotemporal sampling. Clinically available 3D TEE mitral valve assessment tools typically enable segmentation and assessment of a single state of the mitral valve [5–7]. This allows the calculation of quantitative parameters such as annulus perimeter, annulus area, anterior and posterior leaflet area, leaflet length, and tenting height [8] (Fig. 1).

2. Related work

Mitral valve segmentation/reconstruction methods can broadly be classified into three categories: traditional image analysis approaches, simulation-based methods, and deep learning (DL) methods. Each category offers distinct advantages and faces unique challenges, which we review in this section.

Traditional image analysis methods for mitral valve segmentation primarily rely on knowledge-based models and handcrafted features. These include atlas-based methods, which utilize anatomical atlases to guide segmentation [9–11], active surface models, which deform surfaces to fit image data [12], and optical flow-based tracking methods that capture the motion of the valve [13]. Shape models, another traditional approach, represent the valve's geometry using statistical models [14]. While these methods have been foundational in mitral valve analysis, their adaptability to image acquisitions and pathological alterations is limited [15] due to their reliance on predefined features.

Simulation-based methods typically start with valve geometries obtained from traditional image analysis approaches. These simulation-based methods employ biomechanical models and physics-based simulations to predict and analyze the valve's dynamic behavior. These methods can be divided into finite element methods [16–18] and position-based dynamics methods [19]. Finite element-based techniques simulate the mechanical properties and movements of the valve by applying (image-based or physical) forces to an initial geometric reconstruction. Position-based dynamics methods simulate valve dynamics by iterating over positional constraints to maintain mechanical realism. While simulation-based methods offer detailed insights into valve behavior under various conditions, they require an accurate initial geometric model, forces, and material properties, which are not always easy to obtain.

Deep learning (DL) methods can be categorized into voxel-based and mesh-based approaches. Voxel-based methods typically utilize UNet-like architectures to segment the valve from 3D imaging data [20–28]. These methods operate directly on the voxel grid, making them well-suited for handling complex 3D structures. However, one major limitation is the need for dense 3D annotations, which are difficult and expensive to obtain [29]. Moreover, voxel-based segmentation often requires an additional conversion step to produce mesh representations [30] suitable for surgical planning, a process that can introduce topological errors and invalidate the mesh, complicating its use in simulations [31–34]. Mesh-based DL methods, in contrast, focus on directly generating mesh representations of the left ventricle [35] rather than specifically modeling the mitral valve. These approaches bypass some of the challenges associated with voxel-to-mesh conversion by working directly with mesh data. However, these methods are restricted to modeling closed surfaces, which limits their ability to accurately capture the thin, flexible structures of the mitral valve leaflets.

The listed methods vary in their treatment of spatial and temporal dimensions. Some focus on 2D slices, providing limited spatial context, while others operate on single 3D volumes to create a more comprehensive static model. 3D+t methods capture the valve's motion over time, ensuring point correspondence and offering a temporally coherent model. Traditional approaches include gradient-based methods [13,19], which can struggle with fast-moving leaflets, and simple linear models [9,14], which often neglect the non-linear motion of the valve. Simulation-based methods, while capable of detailed temporal analysis [16–18,34], require an initial valve geometry, forces, and a material model to predict dynamics accurately. Additionally, these methods need a chordae model [18], which cannot be easily derived from 3D TEE data.

Our proposed DL method aims to directly infer a high-resolution mesh with inter- and intra-subject point correspondence across various states of the mitral valve from 3D TEE images, using only sparse annotations for training. While existing DL methods are often limited to closed surfaces, our approach is intended to accurately capture the open and flexible structures of the mitral valve leaflets. Additionally, we aim to eliminate the need for predefined material properties, which could simplify application and enhance generalizability across different acquisition techniques, anatomical variations, and pathological conditions. By directly generating a temporally coherent mesh with precise point correspondence, our method aspires to overcome the limitations of current approaches, potentially offering a more robust and accurate tool for mitral valve reconstruction with significant implications for both diagnosis and surgical planning.

3. Dataset

3.1. Image data

The dataset comprises data from 72 subjects. Table 4 shows the distribution of the reported pathology and gender. We selected four images per subject for model training and validation: one with the valve fully open, one fully closed, and two captured during the valve-closing process. This results in 180 3D TEE volumes for training the model and 108 3D TEE volumes for testing. All image sequences were acquired with the GE Vingmed Ultrasound Vivid E9 system at the German Heart Centre of the Charité (DHZC). The temporal resolution is between 12 and 65 ms, the in-plane resolution between 0.47 and 1.43 mm, and the through-plane resolution between 0.33 and 0.98 mm. The image volumes were sparsely annotated by two cardiologists with four and 17 years of experience, utilizing the method proposed by Tautz et al. [36]. Additional information on the dataset is provided in Figure 14 and 15. The leaflets were labeled on nine planes rotated around the axis through the left ventricle's apex and the mitral valve's center (Fig. 1). Landmarks were placed at the annulus, orifice, and on the leaflets.

3.2. Expert annotation

Experts provide sparse point annotations on rotation 2D reformattings of the image volumes. In each rotational plane, experts annotate two annulus points, two orifice points, and multiple leaflet points. In addition, each slice might contain a coaptation point separating the leaflets. These points are connected in order to represent the valve by two lines per rotational multiplanar reformation (MPR) with the Dijkstra shortest path search [37]. The commissures divide the leaflets (and the annotated landmarks) into anterior and posterior. The processing steps for the labeled surface mesh generation are described in the supplements in section 11.1.

4. Method

Mitral Valve Graph Neural Network (MV-GNN) is a supervised end-to-end deep learning method that directly infers a mitral valve surface mesh from 3D TEE imaging data. To facilitate learning from sparse annotations, we create a surface mesh by pre-processing expert-defined landmarks, which are subsequently triangulated (Section 4.1). The resulting mesh is used as a reference for the MV-GNN training described in Section 4.2. We apply this method for each image of the 3D echocardiographic image sequences. Section 4.3 introduces a specialized loss function to guide the model to preserve consistent orientation, the known inlet and outlet, and promote non-self-intersecting valve surfaces. This ensures inter and intra-subject point correspondences across the time series, enabling the derivation of a continuous 3D+t representation of the mitral valve surface, as detailed in Section 4.4. The result is a deep learning method that reconstructs the mitral valve as a 3D+t surface model without expert annotations.

4.1. Mitral valve surface definitions

Topologically, a mitral valve is equivalent to a tube with a single inlet and a single outlet. The open ends can be mapped to the anatomical annulus and orifice contours. We represent the open tube by a prototype mesh, which gets deformed during the network forward pass (as described in Section 4.2). The assignment of these biological structures is illustrated in Fig. 3, with the annulus in blue and orifice vertices in red.

The following notation will be consistently used throughout this section. Let S represent a triangular mesh model of the mitral valve surface, with F denoting the set of faces, E the set of edges, and V the set of vertices in this model. Each vertex $v \in V$ is associated with a 3D coordinate $\vec{x}$, and each face $f \in F$ is characterized by a normal vector $\vec{n}$. Additionally, we define the set of annulus vertices as $A \subset V$ (blue vertices Fig. 3) and the set of orifice vertices as $O \subset V$ (red vertices Fig. 3), corresponding to the vertices belonging to the annulus and orifice, respectively. A subset of six ordered and uniformly spaced landmarks on the annulus, denoted as $V_{ALM} \subset A$, where v_{ALM-1} is the landmark closest to the aorta. S_p and S_r denote the reconstructed (prototype) and reference (expert annotation) mitral valve surface models, respectively, and these subscripts are consistently applied to the corresponding sets such as faces F, edges E, vertices V, annulus A, and orifice O.

4.2. MV-GNN

MV-GNN consists of three main blocks – a voxel encoder, a voxel decoder, and a mesh decoder – illustrated in Fig. 3, similar to the architectures proposed by Wickramasinghe et al. [38],Wang et al. [39],Wen et al. [40],Ivantsits et al. [41]. The voxel encoder and decoder are basic blocks, as proposed in the U-Net paper [42], which compress the data into a latent space (LS) and reverse the process. The prototype mesh for the MV-GNN mesh decoder is a tube with a known inlet and outlet (see Fig. 3). After image encoding, two fully connected (FC) layers are used to establish a rigid registration (RR) that aligns the mesh prototype with the reference mesh. The output of the first layer has 256 parameters, which are then condensed to seven rigid transformation parameters by the second fully connected layer. Three rotational parameters θ_x, θ_y, and θ_z are passed to a hyperbolic tangent activation function and rescaled to a range of $[-\pi, \pi]$. Three translation parameters, t_x, t_y, and t_z, are passed to a Leaky ReLU activation function. A sigmoid activation function is applied to the scaling parameter s. After rigid registration, a local neighborhood sampling (NHS) is applied to each prototype vertex for feature aggregation. A 1D convolution aggregates features from the voxel-decoder space within a sphere of fixed radius. By decreasing the radius linearly while upsampling the voxel space, the considered neighborhood around the vertices becomes smaller, thus reducing the perceptive field. The latent vertex features and the current mesh vertex positions are concatenated and passed to a GNN as proposed by Kipf and Welling [43]. This GNN produces a 3D offset vector for each mesh vertex. The offset is added to the mesh vertex positions generated in the previous resolution step. Next, this mesh is uniformly up-sampled by adding mesh vertices in each edge's center, creating four new faces, which preserves the topology. This process is repeated until the full resolution of the input data is reached. In this process, we generate a surface mesh with 3264 vertices from the initial low-resolution prototype containing 240 vertices.

4.3. Loss design for mitral valve reconstruction training

A specialized loss function is introduced to guide the optimization process, encouraging the generated mitral valve surface to be consistently oriented, non-self-intersecting (Eq. (1), (2), (3)) and has uniformly spaced vertices (Eq. (4)). Additionally, we aim to preserve the positions of the known inlet and outlet vertices (Eq. (5)) and maintain both inter and intra-subject point correspondence (Eq. (8) and (9)).

We define the normal consistency loss

$$\mathcal{L}_{\mathrm{NC}} = \frac{1}{|N_F|} \sum_{(f_0, f_1) \in N_F} 1 - \frac{\vec{n}_0 \cdot \vec{n}_1}{\|\vec{n}_0\| \cdot \|\vec{n}_1\|}, \tag{1}$$

where f_0 and f_1 denote neighboring faces in N_F, the set of all neighboring faces of the reconstructed mesh. $\vec{n}_0$ and $\vec{n}_1$ designate the normal vectors of the neighboring faces.

A Laplacian smoothing constraint

$$\mathcal{L}_{\mathrm{L}} = \frac{1}{|V_p|} \sum_{v \in V_p} \| \frac{1}{|N(v)|} \sum_{v' \in N(v)} (\vec{x} - \vec{x'}) \| \tag{2}$$

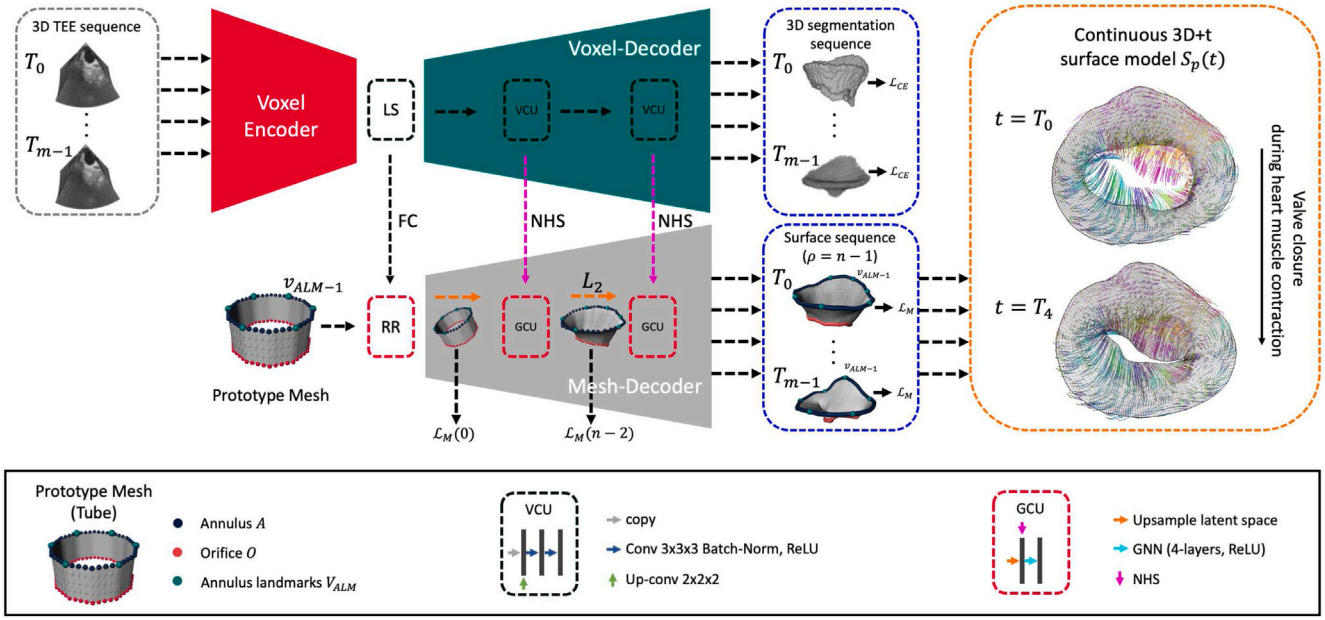

Fig. 3. Model architecture: The network sequentially processes individual 3D image volumes to generate a mitral valve surface mesh. The upper section of the architecture is a conventional U-Net, featuring a voxel encoder and decoder for voxel classification. The lower section incorporates additional components for mesh reconstruction. A rigid transformation is computed from the latent encoder space using a fully connected network. The mesh decoder samples latent features from this space and iteratively refines a prototype mesh at increasing resolutions. During the deformation process, the orientation of edge vertices is preserved, allowing for the accurate reconstruction of the mitral valve, including the annulus and orifice vertices. Key components include VCU (voxel convolution + upsampling), LS (latent space), FC (fully connected layer), RR (rigid registration), NHS (neighborhood sampling), and GCU (graph convolution + upsampling). After reconstructing a sequence of mitral valve surfaces, we use them to derive a continuous 3D+t surface model, denoted as $S_p(t)$. This $S_p(t)$ is an example continuous representation derived from one example.

is applied, where $N(v)$ depicts the set of neighboring vertices of vertex v. Moreover, a face normal loss

$$\mathcal{L}_{\text{MVN}} = \frac{1}{|F_p|} \sum_{(f_p,f_r)\in D_F} 1 - \frac{\vec{n}_p \cdot \vec{n}_r}{\|\vec{n}_p\| \cdot \|\vec{n}_r\|} + \frac{1}{|F_r|} \sum_{(f_r,f_p)\in D_F} 1 - \frac{\vec{n}_p \cdot \vec{n}_r}{\|\vec{n}_p\| \cdot \|\vec{n}_r\|} \tag{3}$$

is introduced, where F_p and F_r depict the sets of faces of the reconstructed and reference mitral valve. D_F is the set of face pairs with minimal distances between the face centers. $\vec{n}_p$ denotes the normal vector of face f_p and $\vec{n}_r$ the normal vector of the closest face f_r to the reconstructed face f_p. This term assesses the similarity of the normal vectors of the reconstructed and reference faces. Eqs. (1), (2), (3) reward a smooth and non-self-intersecting 3D surface reconstruction.

Additionally, we use an edge-length loss

$$\mathcal{L}_{\text{E}} = \frac{1}{|E|} \sum_{(v_0,v_1)\in E} (\|\vec{x}_0 - \vec{x}_1\|_2 - L_t)^2 \tag{4}$$

where E denotes the set of edges of a mesh. v_0 and v_1 are the vertices composing the edge, and L_t (initialized as 0) is defined as a constant target length. In combination with the other loss terms, it penalizes deviations from a target edge length and promotes consistent mesh spacing.

We define the chamfer loss function for a vertex set $M = \{MV, A, O\}$ as

$$\mathcal{L}_{\text{CL}}(M) = \sum_{v_p\in M_p} \min_{v_r\in M_r} \|\vec{x}_p - \vec{x}_r\| + \sum_{v_r\in M_r} \min_{v_p\in M_p} \|\vec{x}_p - \vec{x}_r\|, \tag{5}$$

which calculates the average nearest point distance between the vertices of prototype vertex set M_p and a reference set M_r. The chamfer loss for the mitral valve $\mathcal{L}_{\text{CL}}(MV)$ quantifies the misalignment of the reconstructed surface S_p and the reference created from expert annotations S_r. Similarly, minimizing $\mathcal{L}_{\text{CL}}(A)$ and $\mathcal{L}_{\text{CL}}(O)$ ensures the known inlet and outlet of the reconstructed surface S_p.

We aggregate the loss terms into the set $\Gamma = \{\mathcal{L}_{\text{CL}}(MV), \mathcal{L}_{\text{CL}}(A), \mathcal{L}_{\text{CL}}(O), \mathcal{L}_{\text{E}}, \mathcal{L}_{\text{NC}}, \mathcal{L}_{\text{L}}, \mathcal{L}_{\text{MVN}}\}$. The terms are evaluated for all resolutions $\rho \in R$ at all mesh-decoder stages,

$$\mathcal{L}_M(\rho) = \sum_{\mathcal{L}\in\Gamma} \lambda(\mathcal{L}, \rho)\mathcal{L}(\rho). \tag{6}$$

Each resolution ρ and loss function $\mathcal{L}$ has its own hyperparameter λ. Furthermore, we add a voxel-based cross-entropy loss term $\mathcal{L}_{\text{CE}}$ to the final loss function

$$\mathcal{L}_\gamma = \lambda_{\text{CE}}\mathcal{L}_{\text{CE}} + \sum_{\rho\in R} \mathcal{L}_M(\rho). \tag{7}$$

The cross-entropy loss has its own hyperparameter λ_{CE}.

4.4. Continuous 3D+t mitral valve model generation

The aggregated loss term $\mathcal{L}_\gamma$ guides the reconstruction process to produce a valid 3D mitral valve surface for a single time-point. To enable inter and intra-subject point correspondence, we add two additional loss terms to the set Γ for all resolutions $\rho \in R$. The loss term

$$\mathcal{L}_{\text{ALM}} = \frac{1}{6} \sum_{j=1}^{6} \|\vec{x}'_j - \vec{x}_j\|, \vec{v}'_j \in V'_{ALM}, \vec{v}_j \in V_{ALM} \tag{8}$$

controls the learning of the transformation (RR in Fig. 3) to initialize the prototype mesh. V'_{ALM} represents a set of six ordered and evenly distributed landmarks on the annulus contour. V_{ALM} is the corresponding set of points on the prototype mesh. This initialization ensures that relative vertex positions are comparable across subjects and timeframes.

Additionally, we include an L_2-norm term

$$L_2 = \sum_{v\in S_p} \|\vec{x}(\rho_{i+1}) - \vec{x}(\rho_i)\| \tag{9}$$

to the mesh decoder, where ρ_i and ρ_{i+1}, $i \in \{0, \dots, n-2\}$ are subsequent mesh resolutions (see Fig. 3). This term ensures minimal deformation of the surface in each mesh-decoder step to impose point-correspondence.

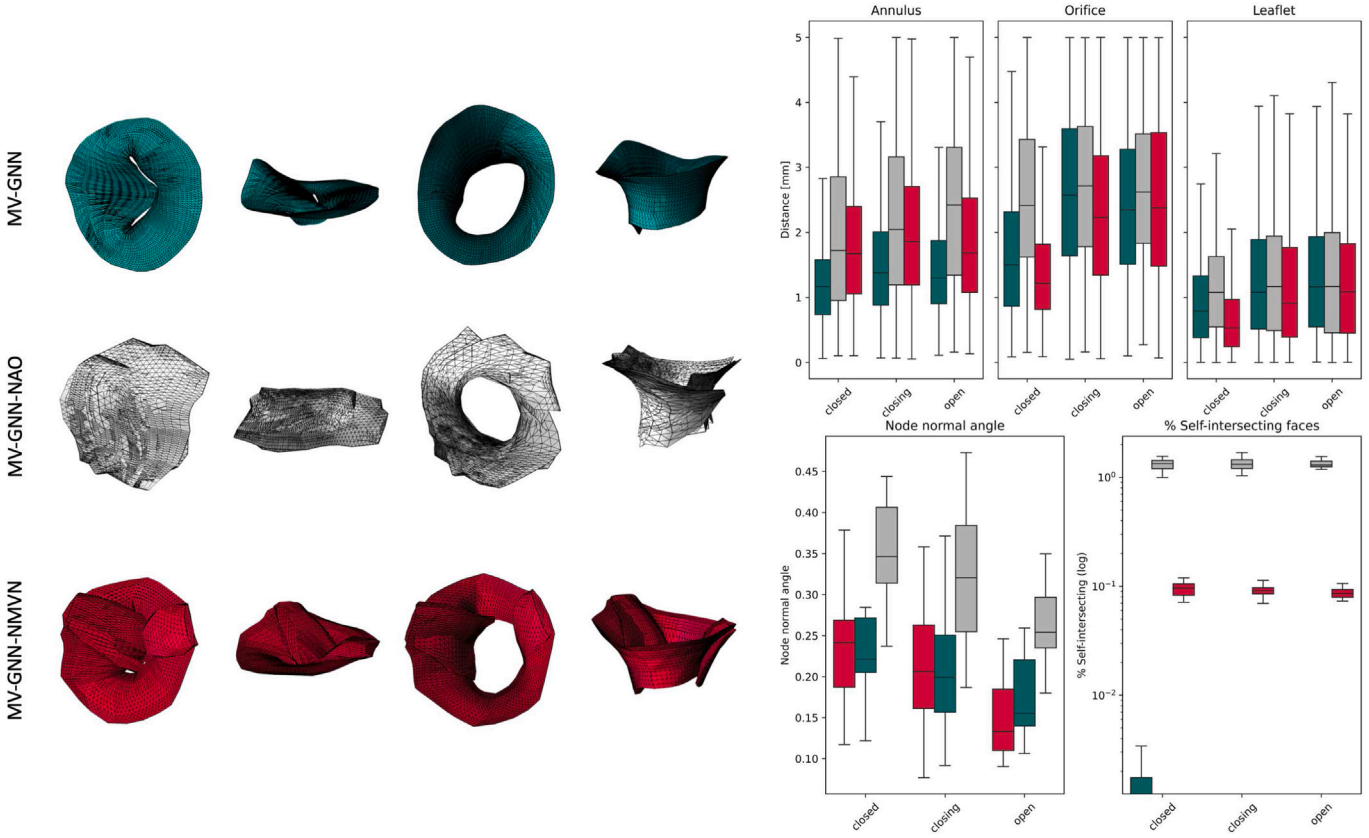

Fig. 4. Qualitative results for valve geometries produced by the MV-GNN, the MV-GNN-NAO (without annulus $\mathcal{L}_{\mathrm{CL}}(A)$ and orifice loss $\mathcal{L}_{\mathrm{CL}}(O)$), and MV-GNN-NMVN (without vertex normal loss $\mathcal{L}_{\mathrm{MVN}}$). We show results for open and closed mitral valve surfaces from a superior and medial view. The top diagrams show the distance distributions on the annulus, orifice, and leaflet for the model trained with the complete loss function, without annulus $\mathcal{L}_{\mathrm{CL}}(A)$ and orifice loss $\mathcal{L}_{\mathrm{CL}}(O)$, and without vertex normal loss $\mathcal{L}_{\mathrm{MVN}}$. The diagram on the bottom left shows the distribution of the vertex normal angles between the expert annotation and MV-GNN surface for the models trained with complete as well as the loss functions without annulus $\mathcal{L}_{\mathrm{CL}}(A)$ and orifice loss $\mathcal{L}_{\mathrm{CL}}(O)$, and without vertex normal loss $\mathcal{L}_{\mathrm{MVN}}$. The diagram on the bottom right shows the distribution for the ratio of self-intersecting faces vs. all faces.

Because of the fixed number of mesh vertices, the initial alignment, and the mesh smoothness conditions, we assume that the corresponding vertex positions in m different timeframes represent the motion trajectories of this vertex. We fit an interpolating quadratic spline to each vertex sequence $v_j(T_i)$, where T_i, $i \in \{0, \ldots, m-1\}$ is the time point and v_j is the consistently numbered vertex in all meshes t_i. Because we can further assume cyclic valve motion, we can thereby derive a continuous representation of the valve geometry over time based on the point correspondence. This approach yields a mitral valve surface $S_p(t)$, $t \in [T_0, T_{m-1}]$, as illustrated in Fig. 3.

5. Model training

We split the sets by subject to avoid information leakage. The training set contains nine healthy volunteers and 36 type I patients. To test the generalizability of the models with regard to valve pathology, we include type II patients during evaluation but not during training. The validation set includes one healthy volunteer, eleven type I patients, and 15 type II patients. All images are re-sampled to an isotropic voxel-spacing of 1.1 mm^3. We perform random affine, blur, and Gaussian noise augmentation during model training. On the 180 training volumes, we perform a five-fold cross-validation (CV) with a grid search to find optimal hyperparameters for the loss weights λ. The final loss hyperparameters are uniformly weighted across all resolutions to limit the search space and save resources. We train on all 180 image volumes with the fixed set of hyperparameters and evaluate the models on the 108 3D TEE volumes test set. The final loss terms are weighted with: $\lambda_{\mathrm{MV}} = 1$, $\lambda_{\mathrm{A}} = 1$, $\lambda_{\mathrm{O}} = 1$, $\lambda_{\mathrm{MVN}} = 0.2$, $\lambda_{\mathrm{L}} = 0.2$, $\lambda_{\mathrm{NC}} = 0.2$, $\lambda_{\mathrm{E}} = 0.2$, $\lambda_{\mathrm{CE}} = 1$, and $\lambda_{\mathrm{ALM}} = 1$. Experiments are performed on an Intel(R) Core(TM) i7-8700K CPU @ 3.70 GHz with 16 GBs RAM and an Nvidia RTX 2080 Ti GPU with 11 GB memory.

6. Ablation study

To analyze the effect of the annulus loss $\mathcal{L}_{\mathrm{CL}}(A)$ and orifice loss $\mathcal{L}_{\mathrm{CL}}(O)$, as well as the mitral valve normal loss $\mathcal{L}_{\mathrm{MVN}}$, we applied the training procedure described in Section 5 with the complete loss function MV-GNN as well with the setups MV-GNN-NAO (without annulus term $\mathcal{L}_{\mathrm{CL}}(A)$ and orifice term $\mathcal{L}_{\mathrm{CL}}(O)$) and MV-GNN-NMVN (without loss term $\mathcal{L}_{\mathrm{MVN}}$). The performance of these models is summarized in Fig. 4. The upper diagram shows the distance distribution from the expert annotations for the annulus, orifice, and leaflet. All three models show similar distance distributions for the leaflet. The MV-GNN-NAO model shows worse annulus distances (2.02 mm) compared to MV-GNN-NMVN (1.79 mm) and MV-GNN (1.31 mm). Furthermore, we observe worse orifice distances for the MV-GNN-NAO (2.66 mm) compared to MV-GNN-NMVN (2.05 mm) and MV-GNN (2.33 mm).

The lower diagram in Fig. 4 displays the vertex normal angles between the expert annotation and segmented surfaces. The model MV-GNN-NMVN trained without vertex normal loss $\mathcal{L}_{\mathrm{MVN}}$ shows stronger mitral valve surface orientation deviations (0.32) compared to MV-GNN-NAO (0.21) and MV-GNN (0.20). The MV-GNN-NAO and MV-GNN-NMVN models exhibit more self-intersections than those trained with the complete loss function. The MV-GNN-NAO exhibits 133% self-intersecting faces, with the MV-GNN-NMVN showing 10% self-intersecting faces. These self-intersections are illustrated on the left of Fig. 4.

Table 1
Overview of the mean distances and standard error in mm for the inter-observer study, the nnUNet, DeepMitral, UNetr, and MV-GNN by pathology and valve state.

Structure	Model	Healthy			Type I			Type II		
		Closed	Closing	Open	Closed	Closing	Open	Closed	Closing	Open
Annulus	MV-GNN	1.52 ± 0.06	1.43 ± 0.03	1.46 ± 0.08	**1.26 ± 0.02**	**1.47 ± 0.02**	**1.41 ± 0.03**	**1.61 ± 0.09**	1.94 ± 0.03	**1.71 ± 0.04**
	Observer	2.04 ± 0.33	1.91 ± 0.18	2.67 ± 0.35	1.91 ± 0.21	1.84 ± 0.15	1.60 ± 0.17	1.99 ± 0.20	1.89 ± 0.12	2.05 ± 0.28
	nnUNet	**1.34 ± 0.19**	**1.41 ± 0.08**	**1.23 ± 0.11**	1.55 ± 0.06	1.66 ± 0.05	1.82 ± 0.08	1.67 ± 0.46	**1.78 ± 0.13**	1.89 ± 0.13
	DeepMitral	3.72 ± 0.50	3.21 ± 0.26	1.63 ± 0.23	5.25 ± 0.45	2.37 ± 0.17	2.18 ± 0.13	5.28 ± 0.48	2.96 ± 0.17	1.92 ± 0.13
	UNetr	1.81 ± 0.46	2.07 ± 0.39	1.74 ± 1.18	1.55 ± 0.08	1.66 ± 0.05	1.73 ± 0.09	1.64 ± 0.28	1.91 ± 0.17	1.86 ± 0.15
Orifice	MV-GNN	2.45 ± 0.09	4.28 ± 0.11	3.67 ± 0.11	1.40 ± 0.04	2.93 ± 0.04	**2.36 ± 0.07**	2.48 ± 0.08	3.34 ± 0.03	**3.19 ± 0.06**
	Observer	2.40 ± 0.33	**2.34 ± 0.22**	3.45 ± 0.43	**1.27 ± 0.34**	**2.36 ± 0.27**	3.19 ± 0.48	**2.08 ± 0.17**	3.45 ± 0.28	3.77 ± 0.52
	nnUNet	**2.36 ± 0.25**	2.58 ± 0.30	**3.18 ± 0.50**	2.22 ± 0.09	2.69 ± 0.13	2.49 ± 0.27	2.27 ± 0.14	**2.91 ± 0.10**	3.20 ± 0.26
	DeepMitral		6.13 ± 0.58	4.05 ± 0.94		3.56 ± 0.19	3.20 ± 0.27		4.06 ± 0.19	4.01 ± 0.25
	UNetr	3.27 ± 0.31	3.76 ± 0.44	6.56 ± 1.47	2.49 ± 0.09	3.08 ± 0.14	3.16 ± 0.30	2.72 ± 0.18	3.39 ± 0.13	4.53 ± 0.35
Leaflet	MV-GNN	0.84 ± 0.02	1.12 ± 0.02	1.19 ± 0.04	**0.63 ± 0.01**	**0.90 ± 0.01**	**0.91 ± 0.02**	0.86 ± 0.02	1.27 ± 0.01	1.32 ± 0.02
	Observer	0.79 ± 0.07	**0.82 ± 0.06**	**0.91 ± 0.11**	1.05 ± 0.06	1.03 ± 0.04	1.42 ± 0.12	0.78 ± 0.06	1.34 ± 0.07	**1.31 ± 0.12**
	nnUNet	0.74 ± 0.07	0.89 ± 0.11	1.89 ± 0.28	0.73 ± 0.03	1.34 ± 0.05	1.55 ± 0.08	0.97 ± 0.08	1.36 ± 0.04	2.14 ± 0.11
	DeepMitral	**0.68 ± 0.07**	1.31 ± 0.13	2.30 ± 0.38	0.68 ± 0.02	1.26 ± 0.05	1.46 ± 0.08	**0.70 ± 0.03**	**1.07 ± 0.03**	2.03 ± 0.09
	UNetr	0.73 ± 0.15	1.31 ± 0.26	5.83 ± 0.97	0.72 ± 0.03	1.45 ± 0.07	1.78 ± 0.10	0.96 ± 0.09	1.44 ± 0.05	2.73 ± 0.13

7. Model performance

To assess the performance of the MV-GNN model, we compared it to state-of-the-art methods from recent literature, namely the DeepMitral approach [23], the UNetr [44], and the nnUNet [45]. Additionally, we perform an inter-observer study.

7.1. DeepMitral, UNetr, and nnUNet

We used the MV-GNN's preprocessing strategy to train and evaluate the DeepMitral and nnUNet models. DeepMitral was trained as suggested by Carnahan et al. [23] over 500 epochs. This method provides a voxel mask for the class valve. Therefore, we voxelized the valve meshes as training input. The nnUNet was trained with the standard 3D configuration, including a 5-fold CV and 1000 epochs. For this model, we trained on four classes: the annulus, orifice, leaflet, and background. Similarly, the UNetr was trained for 1000 epochs on identical classes, using the data augmentation strategy employed for the MV-GNN.

7.2. Quantitative evaluation

Comparing the DeepMitral, UNetr, and nnUNet results requires additional post-processing steps. The segmentation masks are intersected with the rotational MPRs to enable comparison with the expert annotations. From the resulting 2D masks, we extract the leaflet center lines via skeletonization. For the DeepMitral method, we extend this line to extract annulus and orifice points. There is no apparent strategy to extract the orifice for closed valves. The agreement between the model segmentation and the expert annotation is quantified via the distances of the expert annotation points to the skeletonized results.

Nine cases with 45 volumes were available for the inter-observer variability analysis. We calculated the distance of the points marked by observer B to the lines connecting the corresponding points annotated by observer A (see 4.1).

Table 1 summarizes the distances of the second observer annotations as well as the model segmentation/reconstruction results from the annotations by expert A in mm for the annulus, orifice, and leaflet. Additionally, Table 6 presents the p-values from the Kruskal–Wallis test, comparing the best and second-best methods regarding the mean distance to the expert annotation. The observers agree best on healthy volunteer datasets. MV-GNN scores best in the three motion states for patients with Type I pathologies. For patients with Type II pathologies, DeepMitral is slightly better in the *Closed* and *Closing* state. The nnUNet performed best for healthy volunteers. DeepMitral, which did not explicitly consider annulus and orifice labels in training, achieved worse results for corresponding distances. Fig. 5 shows the distribution of the segmentation/reconstruction distances for the different structures.

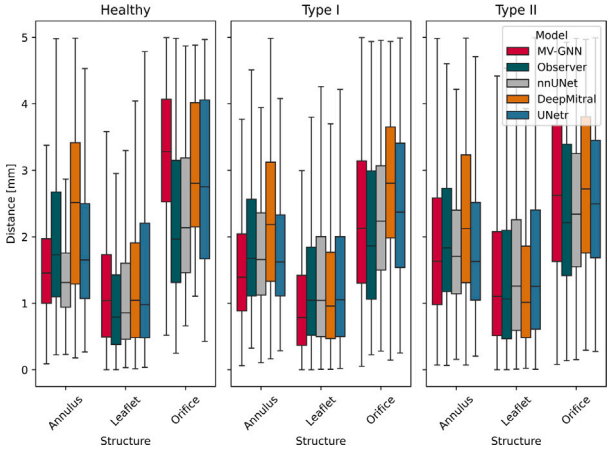

Fig. 5. Surface distances for the inter-observer study, the nnUNet, DeepMitral, UNetr, and our MV-GNN for annulus, orifice, and leaflet by pathology.

Fig. 6 shows MV-GNN reconstructions and expert annotation examples as well as the distance distribution on the valve surface for three Type I cases in *Open*, *Closing*, and *Closed* mitral valve states.

7.3. Point correspondence and continuous representation

The position of the annulus landmarks is essential for achieving anatomical correspondence between reconstruction results of different 3D image volumes. The deviations of the six ordered and equally spaced landmarks on the annulus of the MV-GNN reconstruction are assessed via point distances and rotation angles. Fig. 7 illustrates the landmark distance in mm and the angle in radians with respect to the center of mass of the annulus. We observe an average distance of 2.77 ± 0.24 mm for healthy volunteers, 2.96 ± 0.14 mm for Type I, and 3.25 ± 0.15 mm for Type II pathologies. Furthermore, we observe an average angle deviation of 0.14 ± 0.02 rad for healthy volunteers, 0.12 ± 0.01 rad for Type I, and 0.13 ± 0.01 rad for Type II pathologies.

To examine the continuous 3D+t representation of the valve surface geometry $S_p(t)$, we analyzed an example case consisting of six 3D volumes, T_0, T_1, T_2, T_3, T_4, and T_5. These 3D volume series cover the mitral valve motion from fully open to fully closed. We exclude timeframes T_1 showing valve motion with high velocity and T_4 showing the almost closed valve with minimal motion. The vertex positions in the removed timeframes are then sampled from the spline trajectories introduced in Section 4.4. The point-to-surface distance distribution of the reconstruction-based and interpolation-based meshes is highlighted

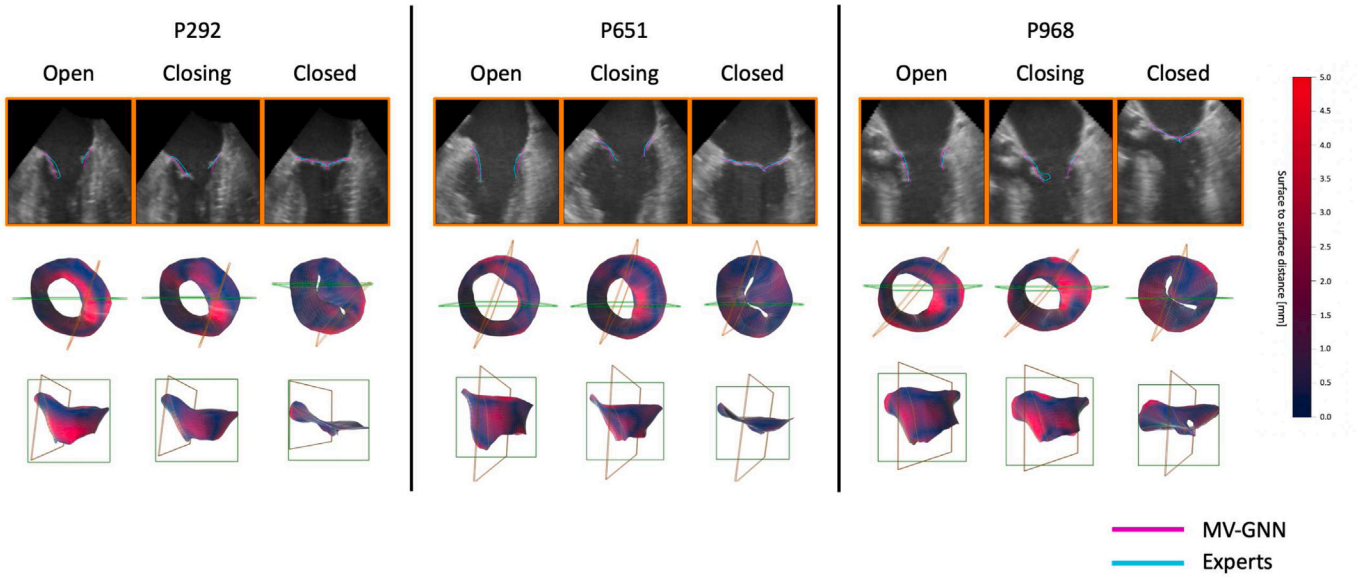

Fig. 6. Visual comparison of the expert annotations and MV-GNN valve models for three selected cases from the test set in fully open, closing, and fully closed valve state. The first row displays 3D TEE image slices picked from the annotation rotation planes. The position relative to the 3D mitral valve is indicated by the orange frame. Rows two and three show the reconstructed mitral valve from a superior and medial view.

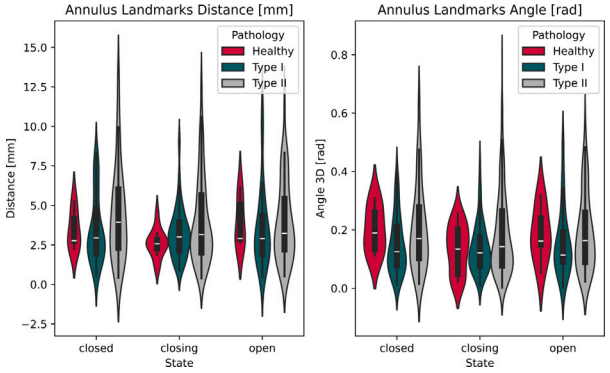

Fig. 7. The diagrams show the deviation distributions of the expert annotation and MV-GNN annulus landmarks. The distance in mm and the angle difference in radians are calculated using the center of mass of the annulus.

Table 2
The average point-to-surface distances in mm of expert annotations to the MV-GNN reconstruction and the reconstruction from the continuous 3D+t representation of the mitral valve for T_1 and T_4.

Structure	Method	T_0	T_1	T_2	T_3	T_4	T_5
Annulus	MV-GNN	1.54	1.12	0.88	0.95	1.01	1.24
	Interpolated		0.94			1.08	
Orifice	MV-GNN	2.27	1.80	3.24	3.06	1.92	1.63
	Interpolated		2.55			2.67	
Leaflet	MV-GNN	0.88	0.85	0.49	0.69	0.48	0.60
	Interpolated		1.18			0.56	

in Table 2. Table 2 shows these distances for $T_0 - T_5$. The average point-to-surface distance for the interpolation method is 1.18 mm for T_1 and 0.56 mm for T_4. The point-to-point distance for the annulus results is 0.94 mm, and 1.08 mm. On the orifice, we observe a point-to-point distance of 2.55 mm and 2.67 mm versus 2.18 mm.

Fig. 8 illustrates reconstruction examples derived from the continuous representation for a patient with Type I pathology. The first row depicts slices from the rotational view on which experts annotated landmarks. The reconstructed mitral valve is displayed in a superior and medial view. Time points T_1 and T_4 are interpolated mitral valve geometries with a mean surface-to-surface distance to the expert's annotation of 1.36 and 0.80 mm respectively.

7.4. Bias analysis for quantitative parameters

We performed a linear regression on the mitral valve area and the maximum annulus diameter to identify biases in the proposed model. For the mitral valve area, we observe an R^2 value of 0.8 for the MV-GNN model vs. expert A and 0.71 for expert B vs expert A. The bias is $-76.09\,\text{mm}^2$ (4.86%) for the MV-GNN model, $172.55\,\text{mm}^2$ (11.02%) for expert B, as illustrated in Fig. 9. The mitral valve area for expert A has a surface area of $(1565.89 \pm 45.89)\,\text{mm}^2$.

Fig. 10 illustrates the bias analysis of the MV-GNN-reconstructed valve regarding the maximum annulus diameter. We observe an R^2 value of 0.6 for MV-GNN vs. expert A and 0.43 for expert B vs. expert A. The bias for MV-GNN is 0.61 mm (1.46%) and 0.48 mm (1.14%) for expert B. The maximum annulus diameter for expert A is $(41.76 \pm 0.43)\,\text{mm}$.

8. Discussion

The presented end-to-end geometric deep-learning approach extracts the mitral valve as a continuous 3D+t surface model using a tube-shaped prototype with labeled mesh vertices representing annulus (inlet), orifice (outlet), and leaflets. Loss terms for annulus, orifice, and vertex normals have been introduced to enforce learning anatomical and typical motion properties. Specific vertices on the annulus are used for rotational alignment to achieve anatomical correspondence of mesh vertices.

8.1. Annulus and orifice

The top diagram of Fig. 4 shows the impact of the annulus and orifice loss. These terms are essential for ensuring a correct leaflet area. However, our bias analysis shown in Fig. 10 reveals an underestimation

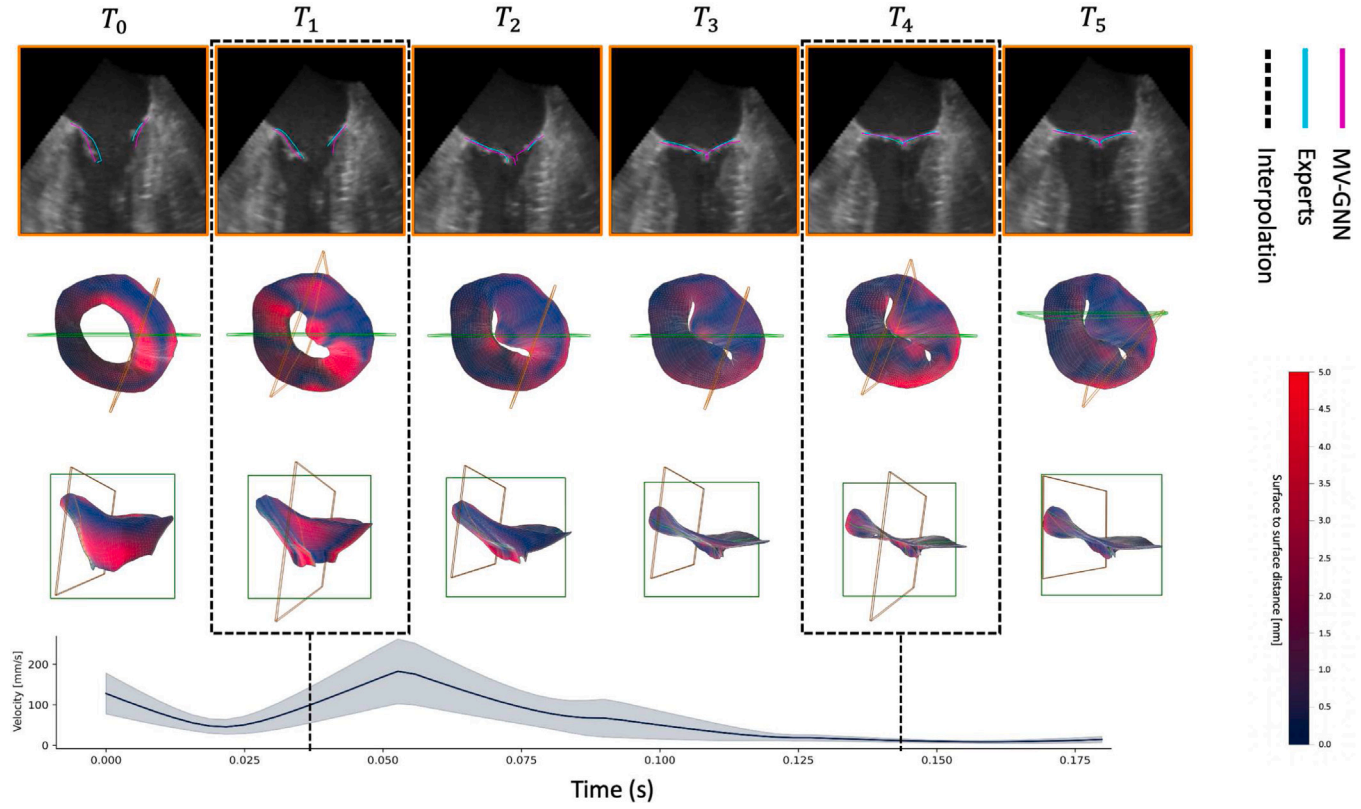

Fig. 8. Comparison of valve representations derived from MV-GNN-derived continuous valve model and expert segmentations. The first row displays a rotational MPR (orange border) showing the mitral valve for six 3D TEE image sequence time frames. Rows two and three show the reconstructed mitral valve from a superior and medial view. The overlaid lines show the expert annotation (cyan) and the MV-GNN model (magenta). The valve model is interpolated for the time frames T_1 and T_4. The curve displays the valve motion velocity derived from the motion trajectories of the continuous valve representation. The distances between the MV-GNN valve model and the expert annotations are smaller for time points with less valve motion. The curve at the bottom illustrates the mean velocity of the valve vertices in mm/s, with the shaded area representing the standard deviation.

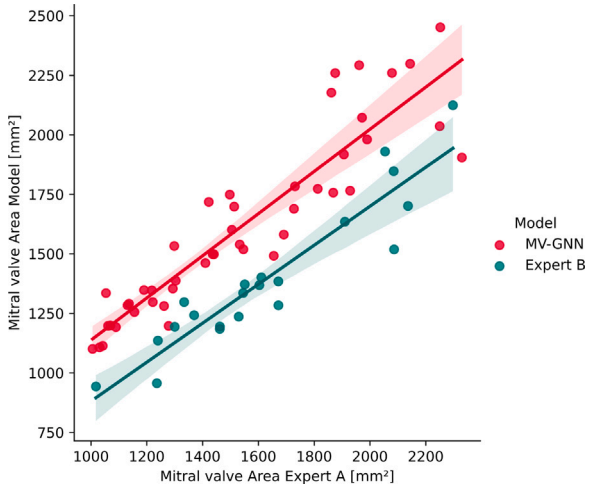

Fig. 9. Bias analysis for the mitral valve surface area. The linear regression of expert A and MV-GNN reconstruction results in an R^2 value of 0.8 and 0.71 for expert B vs. expert A. The bias is $-76.09\,mm^2$ (4.86%) for the MV-GNN model, $172.55\,mm^2$ (11.02%) for expert B.

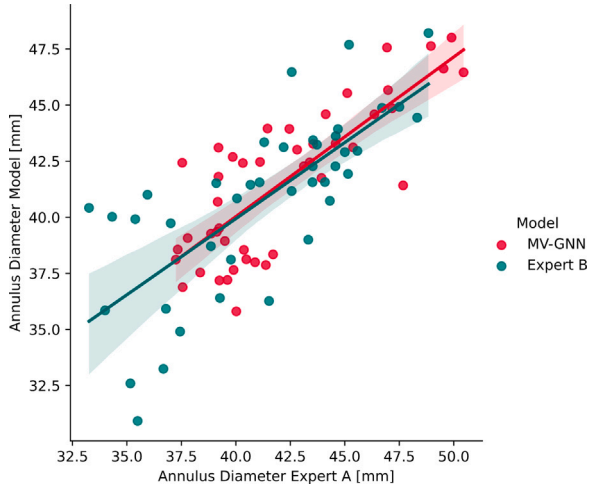

Fig. 10. Bias analysis of the maximum annulus diameter. The linear regression of expert A and MV-GNN results in an R^2 value of 0.6 and 0.43 for expert B vs. expert A. The bias for MV-GNN is 0.61 mm (1.46%) and 0.48 mm (1.14%) for expert B.

of the maximum annulus diameter in the closed state of 4.32 mm (9.97%), 2.76 mm (6.69%) for the closing, and 2.13 mm (4.96%) for the fully open valve. This underestimation is most pronounced for high diameters and less obvious for open valves. For the average point-to-point distance of the annulus, our method is comparable to values reported in related publications for interactive and deep learning-based methods for segmenting the closed valve [27,46].

Table 1 reveals larger deviations across all methods when assessing the orifice in an open valve configuration. This is primarily due to the challenging transition between the orifice and the chordae, which connect the valve leaflets to the papillary muscles (as shown in Fig. 2). Similar discrepancies are evident in the inter-observer study (Table 1),

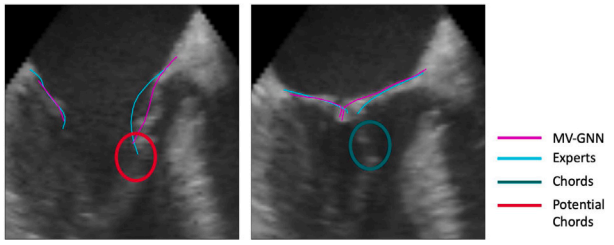

Fig. 11. In the open configuration of the mitral valve, it is often difficult to distinguish the orifice from the chords.

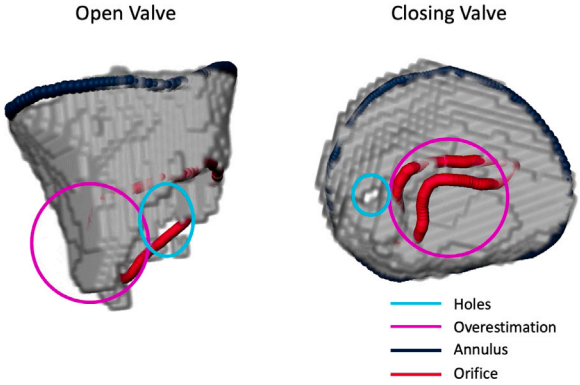

Fig. 12. Two examples of a voxel-based segmentation of the mitral valve with the nnUNet. Left: An open mitral valve with holes and large overestimation around the orifice. Right: A closing valve with holes and overestimation around the orifice producing a closed surface.

indicating the inherent difficulty in this region. Fig. 11 visually highlights this issue, demonstrating that in the closed mitral valve state, the chords are more distinguishable from the leaflet due to the clearer local context. This problem has also been observed in other approaches, such as *DeepMitral* [23], which similarly struggle with this transition.

8.2. Leaflet reconstruction

The results displayed in Fig. 4 for the MV-GNN-NMVN show the influence of the normal loss term, which helps to train the model to avoid mitral valve leaflet intersections that could not occur during the cardiac cycle. This effect is quantitatively confirmed by the decreased mesh vertex normal angle deviations and mesh face intersections.

Fig. 9 reveals a bias with an underestimation of the MV-GNN reconstructed surface area of $-76.09\,\mathrm{mm}^2$ (4.86%). This can be explained by more curvature in the reference valves seen in Fig. 6. Regarding valve surface area bias, our MV-GNN slightly outperforms the Deep Learning approach by Munafo et al. [27] and the bias of expert B vs. expert A (Fig. 9).

Our approach generates a surface representation, which is ideal for dynamics analysis and simulation input but neglects tissue thickness, which is required for the assessment of thickening or calcification. Voxel-based approaches can overcome these restrictions but typically neglect prior knowledge about segmented objects' anatomical and topological properties. Furthermore, being fundamentally a prototype/template fit, our method has inherent limitations; it cannot accurately replicate pathological alterations such as torn leaflets without modifications to the network architecture.

Fig. 12 shows two examples of segmentations produced by the nnUNet. Although the segmentation metrics shown in Table 1 illustrate good results, we observe implausible valve properties, such as non-existing connections between separate leaflets and holes in the leaflets. In voxel-based approaches, the generation of continuous valve surfaces is addressed in an additional post-processing step [23,26,27]. As shown in Fig. 3, the proposed architecture can output both mesh and voxel-based segmentation and, therefore, enables the combined analysis to overcome the limitations of the separate approaches.

Training and evaluation of our approach are based on expert annotations. The inter-observer variability study in Table 1 and related studies [19,46] are in a similar range as the difference between expert segmentations and the results of our method. The results shown in Table 1 are comparable to values reported for voxel-based segmentation methods for the average point-to-surface leaflet distance from expert annotations [9,12,16,23,26,27,46].

8.3. Continuous 3D+t mitral valve surface representation

Table 2 and 8 show promising results of applying the 3D+t continuous mitral valve representation for temporal interpolation. T_1 in Table 2 and 8 shows a slightly reduced point-to-surface distance on the interpolation than the MV-GNN image-based method. The error on T_4 is in a similar range due to less motion during this phase of the valve closure. Compared to the multi-atlas-based method by Pouch et al. [9], which also considers temporal continuity, the proposed approach requires fewer processing steps.

9. Conclusion

We presented an end-to-end deep learning-based method for reconstructing the mitral valve from 3D TEE data, providing a continuous 3D+t model for mitral valve motion analysis. Our approach overcomes limitations in traditional DL models by utilizing a mesh representation to construct a topologically accurate 3D+t mitral valve model, offering robustness and accuracy in approximating the sparse data. Our continuous representation may allow us to acquire higher spatial and lower temporal resolution images.

The model can be applied to analyze the local dynamics of the anterior and posterior leaflets and further give insights into the motion of the leaflets' sub-segments. Interactive methods [47] to infer chord configurations might be automated through combination with our approach. Additionally, 3D+t representations of the valve can be combined with sophisticated analysis and visualization methods [48] to enable domain experts to analyze the valve motion of the cardiac cycle. Extensions might include a vertex classification of the reconstructed 3D surface.

Funding

This work was partly supported by the German Ministry for Education and Research Grant MINIMAKI: 16SV8649.

CRediT authorship contribution statement

Matthias Ivantsits: Writing – review & editing, Writing – original draft, Visualization, Validation, Software, Methodology, Formal analysis, Conceptualization. **Lennart Tautz:** Data curation, Conceptualization. **Markus Huellebrand:** Conceptualization. **Lars Walczak:** Writing – review & editing, Formal analysis. **Serdar Akansel:** Data curation. **Inna Khasyanova:** Data curation. **Jörg Kempfert:** Resources, Data curation. **Simon Sündermann:** Resources, Data curation. **Volkmar Falk:** Resources. **Anja Hennemuth:** Writing – review & editing, Writing – original draft, Supervision, Resources, Funding acquisition, Conceptualization.

Declaration of competing interest

The authors declare the following financial interests/personal relationships which may be considered as potential competing interests: Matthias Ivantsits reports financial support was provided by German Ministry for Education and Research. If there are other authors, they declare that they have no known competing financial interests or personal relationships that could have appeared to influence the work reported in this paper.

Acknowledgments

We would like to extend our deepest thanks to Ann Laube and Chiara Manini for their thorough and meticulous proofreading of this paper, which greatly improved the clarity and readability of the manuscript.

Appendix A. Supplementary data

Supplementary material related to this article can be found online at https://doi.org/10.1016/j.compbiomed.2024.109154.

References

[1] A. Carpentier, Cardiac valve surgery—the "french correction", J. Thorac. Cardiovasc. Surg. 86 (3) (1983) 323–337, http://dx.doi.org/10.1016/S0022-5223(19)39144-5, URL https://www.sciencedirect.com/science/article/pii/S0022522319391445.

[2] R.A. Nishimura, C.M. Otto, R.O. Bonow, B.A. Carabello, J.P. Erwin III, L.A. Fleisher, H. Jneid, M.J. Mack, C.J. McLeod, P.T. O'Gara, V.H. Rigolin, T.M. Sundt III, A. Thompson, 2017 AHA/ACC focused update of the 2014 AHA/ACC guideline for the management of patients with valvular heart disease: A report of the American college of cardiology/American heart association task force on clinical practice guidelines, Circulation 135 (25) (2017) e1159–e1195, http://dx.doi.org/10.1161/cir.0000000000000503, URL https://www.ahajournals.org/doi/pdf/10.1161/CIR.0000000000000503?download=true, 1524-4539 Nishimura, Rick A Otto, Catherine M Bonow, Robert O Carabello, Blase A Erwin, John P 3rd Fleisher, Lee A Jneid, Hani Mack, Michael J McLeod, Christopher J O'Gara, Patrick T Rigolin, Vera H Sundt, Thoralf M 3rd Thompson, Annemarie Journal Article Review United States Circulation. 2017 Jun 20;135(25):e1159-e1195. doi: 10.1161/CIR.0000000000000503. Epub 2017 Mar 15.

[3] L.E. de Groot-de Laat, J. McGhie, B. Ren, R. Frowijn, F.B. Oei, M.L. Geleijnse, A modified echocardiographic classification of mitral valve regurgitation mechanism: The role of three-dimensional echocardiography, J Cardiovasc Imaging 27 (3) (2019) 187–199, http://dx.doi.org/10.4250/jcvi.2019.27.e29, URL https://www.ncbi.nlm.nih.gov/pmc/articles/PMC6669177/pdf/jcvi-27-187.pdf, 2586-7296 de Groot-de Laat, Lotte E Orcid: 0000-0001-9821-9569 McGhie, Jackie Orcid: 0000-0001-6359-4115 Ren, Ben Orcid: 0000-0002-8227-8094 Frowijn, René Orcid: 0000-0002-6214-008x Oei, Frans B Orcid: 0000-0003-2412-0026 Geleijnse, Marcel L Orcid: 0000-0002-0941-3384 Journal Article Review Korea (South) J Cardiovasc Imaging. 2019 Jul;27(3):187-199. doi: 10.4250/jcvi.2019.27.e29. Epub 2019 May 13.

[4] M. Penso, M. Pepi, V. Mantegazza, C. Cefalù, M. Muratori, L. Fusini, P. Gripari, S. Ghulam Ali, E.G. Caiani, G. Tamborini, Machine learning prediction models for mitral valve repairability and mitral regurgitation recurrence in patients undergoing surgical mitral valve repair, Bioengineering (Basel) 8 (9) (2021) http://dx.doi.org/10.3390/bioengineering8090117, 2306-5354 Penso, Marco Orcid: 0000-0003-4040-6112 Pepi, Mauro Mantegazza, Valentina Orcid: 0000-0002-0696-1625 Cefalù, Claudia Muratori, Manuela Fusini, Laura Orcid: 0000-0003-0309-6231 Gripari, Paola Ghulam Ali, Sarah Caiani, Enrico G Orcid: 0000-0002-1770-6486 Tamborini, Gloria Journal Article Switzerland 2021/09/26 Bioengineering (Basel). 2021 Aug 25;8(9):117. doi: 10.3390/bioengineering8090117.

[5] S.L. Gonzalez Navarrete, J.A. de Agustin Loeches, E. Pozo Osinalde, K. de Jesus, A. Madrigal, S.L. Lopez, E. Ortiz, A. Saltijeral, E. Enriquez-Rodriguez, J.J. Gomez de Diego, P. Mahia, P. Marcos Alberca, M.A. Garcia Fernandez, C. Macaya, L. Perez de Isla, Mitral valve navigator. a new diagnostic tool for effective regurgitant orifice quantification in mitral regurgitation, Echocardiography 35 (11) (2018) 1812–1817, http://dx.doi.org/10.1111/echo.14114, https://www.ncbi.nlm.nih.gov/pubmed/30079468 https://onlinelibrary.wiley.com/doi/10.1111/echo.14114, Gonzalez Navarrete, Sandra L de Agustin Loeches, Jose Alberto Pozo Osinalde, Eduardo de Jesus, Keyla Madrigal, Adahir Lopez, Silvana L Ortiz, Eduardo Saltijeral, Adriana Enriquez-Rodriguez, Eduardo Gomez de Diego, Jose J Mahia, Patricia Marcos Alberca, Pedro Garcia Fernandez, Miguel A Macaya, Carlos Perez de Isla, Leopoldo eng Echocardiography. 2018 Nov;35(11):1812-1817. doi: 10.1111/echo.14114. Epub 2018 Aug 5.

[6] F. Veronesi, G. Lie, S. Rabben, 4D auto MVQ, 2017, None.

[7] Tomtec, 4D MV-assessment, 2018, None.

[8] L. Ryan, B. Jackson, L. Parish, H. Sakamoto, T. Plappert, M.S. Sutton, J. Gorman III, R. Gorman, Quantification and localization of mitral valve tenting in ischemic mitral regurgitation using real-time three-dimensional echocardiography, Eur. J. Cardiothorac Surg. 31 (5) (2007) 839–844, http://dx.doi.org/10.1016/j.ejcts.2007.01.050, URL https://pubmed.ncbi.nlm.nih.gov/17329114/.

[9] A.M. Pouch, A.H. Aly, E.K. Lai, N. Yushkevich, R.H. Stoffers, J.H.t. Gorman, A.T. Cheung, J.H. Gorman III, R.C. Gorman, P.A. Yushkevich, Spatiotemporal segmentation and modeling of the mitral valve in real-time 3D echocardiographic images, Med. Image Comput. Comput. Assist. Interv. 10433 (2017) 746–754, http://dx.doi.org/10.1007/978-3-319-66182-7_85, URL https://www.ncbi.nlm.nih.gov/pmc/articles/PMC5743331/pdf/nihms906922.pdf.

[10] A.H. Aly, A.H. Aly, M. Elrakhawy, K. Haroun, L. Prieto-Riascos, R.C. Gorman Jr., N. Yushkevich, Y. Saito, J.H. Gorman III, R.C. Gorman, P.A. Yushkevich, A.M. Pouch, Semi-automated image segmentation of the midsystolic left ventricular mitral valve complex in ischemic mitral regurgitation, Stat Atlases Comput. Model Heart 11395 (2019) 142–151, http://dx.doi.org/10.1007/978-3-030-12029-0_16, URL https://www.ncbi.nlm.nih.gov/pmc/articles/PMC6774645/pdf/nihms-1050974.pdf.

[11] A.H. Aly, A.H. Aly, E.K. Lai, N. Yushkevich, R.H. Stoffers, J.H. Gorman, A.T. Cheung, J.H. Gorman, R.C. Gorman, P.A. Yushkevich, A.M. Pouch, In vivo image-based 4D modeling of competent and regurgitant mitral valve dynamics, Exp. Mech. 61 (1) (2021) 159–169, http://dx.doi.org/10.1007/s11340-020-00656-8.

[12] P. Carnahan, O. Ginty, J. Moore, A. Lasso, M.A. Jolley, C. Herz, M. Eskandari, D. Bainbridge, T.M. Peters, Interactive-automatic segmentation and modelling of the mitral valve, in: Y. Coudière, V. Ozenne, E. Vigmond, N. Zemzemi (Eds.), Functional Imaging and Modeling of the Heart, Springer International Publishing, pp. 397–404.

[13] R.J. Schneider, N.A. Tenenholtz, D.P. Perrin, G.R. Marx, P.J. del Nido, R.D. Howe, Patient-specific mitral leaflet segmentation from 4D ultrasound, Med. Image Comput. Comput. Assist. Interv. 14 (Pt 3) (2011) 520–527, http://dx.doi.org/10.1007/978-3-642-23626-6_64.

[14] F.M. Weber, T. Stehle, I. Waechter-Stehle, M. Götz, J. Peters, S. Mollus, J. Balzer, M. Kelm, J. Weese, Analysis of mitral valve motion in 4D transesophageal echocardiography for transcatheter aortic valve implantation, in: O. Camara, T. Mansi, M. Pop, K. Rhode, M. Sermesant, A. Young (Eds.), Statistical Atlases and Computational Models of the Heart - Imaging and Modelling Challenges, Springer International Publishing, pp. 168–176.

[15] M.E. Rayed, S.M.S. Islam, S.I. Niha, J.R. Jim, M.M. Kabir, M.F. Mridha, Deep learning for medical image segmentation: State-of-the-art advancements and challenges, Inform. Med. Unlocked 47 (2024) 101504, http://dx.doi.org/10.1016/j.imu.2024.101504, URL https://www.sciencedirect.com/science/article/pii/S2352914824000601.

[16] P. Burlina, C. Sprouse, D. DeMenthon, A. Jorstad, R. Juang, F. Contijoch, T. Abraham, D. Yuh, E. McVeigh, Patient-specific modeling and analysis of the mitral valve using 3D-TEE, in: N. Navab, P. Jannin (Eds.), Information Processing in Computer-Assisted Interventions, Springer Berlin Heidelberg, pp. 135–146.

[17] N.T. Simonian, H. Liu, A.M. Pouch, J.H. Gorman III, R.C. Gorman, M.S. Sacks, Quantitative in vivo assessment of human mitral valve coaptation area after undersized ring annuloplasty repair for ischemic mitral regurgitation, JTCVS Tech. 16 (2022) 49–59, http://dx.doi.org/10.1016/j.xjtc.2022.09.013, 2666-2507 Simonian, Natalie T Liu, Hao Pouch, Alison M Gorman, Joseph H 3rd Gorman, Robert C Sacks, Michael S F31 HL170754/HL/NHLBI NIH HHS/United States Journal Article United States 2022/12/14 JTCVS Tech. 2022 Oct 1;16:49-59. doi: 10.1016/j.xjtc.2022.09.013. eCollection 2022 Dec.

[18] S. Grbic, T.F. Easley, T. Mansi, C.H. Bloodworth, E.L. Pierce, I. Voigt, D. Neumann, J. Krebs, D.D. Yuh, M.O. Jensen, D. Comaniciu, A.P. Yoganathan, Personalized mitral valve closure computation and uncertainty analysis from 3D echocardiography, Med. Image Anal 35 (2017) 238–249, http://dx.doi.org/10.1016/j.media.2016.03.011, 1361-8423 Grbic, Sasa Easley, Thomas F Mansi, Tommaso Bloodworth, Charles H Pierce, Eric L Voigt, Ingmar Neumann, Dominik Krebs, Julian Yuh, David D Jensen, Morten O Comaniciu, Dorin Yoganathan, Ajit P Journal Article Netherlands 2016/08/01 Med Image Anal. 2017 Jan;35:238-249. doi: 10.1016/j.media.2016.03.011. Epub 2016 May 17.

[19] L. Tautz, L. Walczak, J. Georgii, A. Jazaerli, K. Vellguth, I. Wamala, S. Sündermann, V. Falk, A. Hennemuth, Combining position-based dynamics and gradient vector flow for 4d mitral valve segmentation in TEE sequences, Int. J. Comput. Assist. Radiol. Surg. 15 (1) (2020) 119–128, http://dx.doi.org/10.1007/s11548-019-02071-4.

[20] H. Dröge, B. Yuan, R. Llerena, J.T. Yen, M. Moeller, A.L. Bertozzi, Mitral valve segmentation using robust nonnegative matrix factorization, J Imaging 7 (10) (2021) http://dx.doi.org/10.3390/jimaging7100213, 2313-433x Dröge, Hannah Orcid: 0000-0001-7163-4279 Yuan, Baichuan Llerena, Rafael Yen, Jesse T Moeller, Michael Bertozzi, Andrea L Journal Article Switzerland 2021/10/23 J Imaging. 2021 Oct 16;7(10):213. doi: 10.3390/jimaging7100213.

[21] L. Corinzia, F. Laumer, A. Candreva, M. Taramasso, F. Maisano, J.M. Buhmann, Neural collaborative filtering for unsupervised mitral valve segmentation in echocardiography, Artif. Intell. Med. 110 (2020) 101975, http://dx.doi.org/10.1016/j.artmed.2020.101975, URL https://www.sciencedirect.com/science/article/pii/S0933365720312409.

[22] E. Costa, N. Martins, M.S. Sultan, D. Veiga, M. Ferreira, S. Mattos, M. Coimbra, Mitral valve leaflets segmentation in echocardiography using convolutional neural networks, in: 2019 IEEE 6th Portuguese Meeting on Bioengineering, ENBENG, pp. 1–4, http://dx.doi.org/10.1109/ENBENG.2019.8692573, URL https://ieeexplore.ieee.org/document/8692573/.

[23] P. Carnahan, J. Moore, D. Bainbridge, M. Eskandari, E.C.S. Chen, T.M. Peters, DeepMitral: Fully automatic 3D echocardiography segmentation for patient specific mitral valve modelling, in: M. de Bruijne, P.C. Cattin, S. Cotin, N. Padoy, S. Speidel, Y. Zheng, C. Essert (Eds.), Medical Image Computing and Computer Assisted Intervention – MICCAI 2021, Springer International Publishing, pp. 459–468.

[24] A.H. Aly, P. Khandelwal, A.H. Aly, T. Kawashima, K. Mori, Y. Saito, J. Hung, J.H. Gorman III, A.M. Pouch, R.C. Gorman, P.A. Yushkevich, Fully automated 3D segmentation and diffeomorphic medial modeling of the left ventricle mitral valve complex in ischemic mitral regurgitation, Med. Image Anal. 80 (2022) 102513, http://dx.doi.org/10.1016/j.media.2022.102513, 1361-8423 Aly, Ahmed H Khandelwal, Pulkit Aly, Abdullah H Kawashima, Takayuki Mori, Kazuki Saito, Yoshiaki Hung, Judy Gorman, Joseph H 3rd Pouch, Alison M Gorman, Robert C Yushkevich, Paul A R01 HL103723/HL/NHLBI NIH HHS/United States F30 HL142138/HL/NHLBI NIH HHS/United States Journal Article Research Support, N.I.H., Extramural Netherlands 2022/07/01 Med Image Anal. 2022 Aug;80:102513. doi: 10.1016/j.media.2022.102513. Epub 2022 Jun 12.

[25] H. Huang, Z. Ge, H. Wang, J. Wu, C. Hu, N. Li, X. Wu, C. Pan, Segmentation of echocardiography based on deep learning model, Electronics 11 (11) (2022) 1714, URL https://www.mdpi.com/2079-9292/11/11/1714.

[26] J. Chen, H. Li, G. He, F. Yao, L. Lai, J. Yao, L. Xie, Automatic 3D mitral valve leaflet segmentation and validation of quantitative measurement, Biomed. Signal Process. Control 79 (2023) http://dx.doi.org/10.1016/j.bspc.2022.104166, URL https://www.sciencedirect.com/science/article/abs/pii/S1746809422006206?via%3Dihub.

[27] R. Munafo, S. Saitta, G. Ingallina, P. Denti, F. Maisano, E. Agricola, A. Redaelli, E. Votta, A deep learning-based and fully automated pipeline for regurgitant mitral valve anatomy analysis from 3D echocardiography, 2023, arXiv e-prints.

[28] S.V. Wifstad, H.A. Kildahl, B. Grenne, E. Holte, S.W. Hauge, S. Sæbø, D. Mekonnen, B. Nega, R. Haaverstad, M.-E. Estensen, H. Dalen, L. Lovstakken, Mitral valve segmentation and tracking from transthoracic echocardiography using deep learning, Ultrasound Med. Biol. 50 (5) (2024) 661–670, http://dx.doi.org/10.1016/j.ultrasmedbio.2023.12.023.

[29] J. Brosig, N. Krüger, I. Khasyanova, I. Wamala, M. Ivantsits, S. Sündermann, J. Kempfert, S. Heldmann, A. Hennemuth, Learning three-dimensional aortic root assessment based on sparse annotations, J. Med. Imaging (Bellingham) 11 (4) (2024) 044504, http://dx.doi.org/10.1117/1.Jmi.11.4.044504, 2329-4310 Brosig, Johanna Orcid: 0009-0003-4212-647x Krüger, Nina Orcid: 0000-0002-2688-9480 Khasyanova, Inna Orcid: 0000-0002-5839-8504 Wamala, Isaac Ivantsits, Matthias Orcid: 0000-0003-0317-7154 Sündermann, Simon Kempfert, Jörg Heldmann, Stefan Hennemuth, Anja Orcid: 0000-0002-0737-7375 Journal Article United States 2024/08/01 J Med Imaging (Bellingham). 2024 Jul;11(4):044504. doi: 10.1117/1.JMI.11.4.044504. Epub 2024 Jul 30.

[30] P. Frey, P.-L. George, Mesh generation, in: Mesh Generation, 2008, pp. 275–302, http://dx.doi.org/10.1002/9780470611166.ch8.

[31] T. Mansi, I. Voigt, B. Georgescu, X. Zheng, E.A. Mengue, M. Hackl, R.I. Ionasec, T. Noack, J. Seeburger, D. Comaniciu, An integrated framework for finite-element modeling of mitral valve biomechanics from medical images: application to MitralClip intervention planning, Med. Image Anal. 16 (7) (2012) 1330–1346, http://dx.doi.org/10.1016/j.media.2012.05.009, 1361-8423 Mansi, Tommaso Voigt, Ingmar Georgescu, Bogdan Zheng, Xudong Mengue, Etienne Assoumou Hackl, Michael Ionasec, Razvan I Noack, Thilo Seeburger, Joerg Comaniciu, Dorin Journal Article Netherlands 2012/07/07 Med Image Anal. 2012 Oct;16(7):1330-46. doi: 10.1016/j.media.2012.05.009. Epub 2012 Jun 13.

[32] A. Drach, A.H. Khalighi, M.S. Sacks, A comprehensive pipeline for multi-resolution modeling of the mitral valve: V alidation, computational efficiency, and predictive capability, Int. J. Numer. Methods Biomed. Eng. 34 (2) (2018) e2921.

[33] M. Peirlinck, F.S. Costabal, J. Yao, J.M. Guccione, S. Tripathy, Y. Wang, D. Ozturk, P. Segars, T.M. Morrison, S. Levine, E. Kuhl, Precision medicine in human heart modeling, Biomech. Model. Mechanobiol. 20 (3) (2021) 803–831, http://dx.doi.org/10.1007/s10237-021-01421-z.

[34] L. Walczak, J. Georgii, L. Tautz, M. Neugebauer, I. Wamala, S. Sündermann, V. Falk, A. Hennemuth, Using position-based dynamics for simulating mitral valve closure and repair procedures, Comput. Graph. Forum 41 (1) (2022) 270–287, http://dx.doi.org/10.1111/cgf.14434, https://onlinelibrary.wiley.com/doi/abs/10.1111/cgf.14434 https://onlinelibrary.wiley.com/doi/pdfdirect/10.1111/cgf.14434?download=true.

[35] F. Kong, N. Wilson, S. Shadden, A deep-learning approach for direct whole-heart mesh reconstruction, Med. Image Anal. 74 (2021) 102222, http://dx.doi.org/10.1016/j.media.2021.102222, URL https://www.sciencedirect.com/science/article/pii/S136184152100267X.

[36] L. Tautz, M. Neugebauer, M. Hüllebrand, K. Vellguth, F. Degener, S. Sündermann, I. Wamala, L. Goubergrits, T. Kuehne, V. Falk, A. Hennemuth, Extraction of open-state mitral valve geometry from CT volumes, Int. J. Comput. Assist. Radiol. Surg. 13 (11) (2018) 1741–1754, http://dx.doi.org/10.1007/s11548-018-1831-6, URL https://link.springer.com/article/10.1007/s11548-018-1831-6, 1861-6429 Tautz, Lennart Neugebauer, Mathias Hüllebrand, Markus Vellguth, Katharina Degener, Franziska Sündermann, Simon Wamala, Isaac Goubergrits, Leonid Kuehne, Titus Falk, Volkmar Hennemuth, Anja 03VP00852/Bundesministerium für Bildung und Forschung (DE)/ Journal Article Germany 2018/08/04 Int J Comput Assist Radiol Surg. 2018 Nov;13(11):1741-1754. doi: 10.1007/s11548-018-1831-6. Epub 2018 Aug 3.

[37] E.W. Dijkstra, A note on two problems in connexion with graphs, Numer. Math. 1 (1) (1959) 269–271, http://dx.doi.org/10.1007/BF01386390.

[38] U. Wickramasinghe, E. Remelli, G. Knott, P. Fua, Voxel2Mesh: 3D mesh model generation from volumetric data, in: A.L. Martel, P. Abolmaesumi, D. Stoyanov, D. Mateus, M.A. Zuluaga, S.K. Zhou, D. Racoceanu, L. Joskowicz (Eds.), Medical Image Computing and Computer Assisted Intervention – MICCAI 2020, Springer International Publishing, pp. 299–308.

[39] N. Wang, Y. Zhang, Z. Li, Y. Fu, W. Liu, Y.-G. Jiang, Pixel2Mesh: Generating 3D mesh models from single RGB images, in: V. Ferrari, M. Hebert, C. Sminchisescu, Y. Weiss (Eds.), Computer Vision – ECCV 2018, Springer International Publishing, pp. 55–71.

[40] C. Wen, Y. Zhang, Z. Li, Y. Fu, Pixel2Mesh++: Multi-view 3D mesh generation via deformation, in: 2019 IEEE/CVF International Conference on Computer Vision, ICCV, pp. 1042–1051, http://dx.doi.org/10.1109/ICCV.2019.00113, URL https://ieeexplore.ieee.org/document/9010697/.

[41] M. Ivantsits, B. Pfahringer, M. Huellebrand, L. Walczak, L. Tautz, O. Nemchyna, S. Akansel, J. Kempfert, S. Sündermann, A. Hennemuth, 3D mitral valve surface reconstruction from 3D TEE via graph neural networks, in: O. Camara, E. Puyol-Antón, C. Qin, M. Sermesant, A. Suinesiaputra, S. Wang, A. Young (Eds.), Statistical Atlases and Computational Models of the Heart. Regular and CMRxMotion Challenge Papers, Springer Nature Switzerland, pp. 330–339.

[42] O. Ronneberger, P. Fischer, T. Brox, U-net: Convolutional networks for biomedical image segmentation, in: N. Navab, J. Hornegger, W.M. Wells, A.F. Frangi (Eds.), Medical Image Computing and Computer-Assisted Intervention – MICCAI 2015, Springer International Publishing, pp. 234–241.

[43] T.N. Kipf, M. Welling, Semi-supervised classification with graph convolutional networks, 2016, http://dx.doi.org/10.48550/arXiv.1609.02907, arXiv e-prints https://ui.adsabs.harvard.edu/abs/2016arXiv160902907K https://arxiv.org/pdf/1609.02907.pdf.

[44] A. Hatamizadeh, Y. Tang, V. Nath, D. Yang, A. Myronenko, B. Landman, H.R. Roth, D. Xu, UNETR: Transformers for 3D medical image segmentation, in: 2022 IEEE/CVF Winter Conference on Applications of Computer Vision, WACV, pp. 1748–1758, http://dx.doi.org/10.1109/WACV51458.2022.00181.

[45] F. Isensee, P.F. Jaeger, S.A.A. Kohl, J. Petersen, K.H. Maier-Hein, Nnu-net: a self-configuring method for deep learning-based biomedical image segmentation, Nature Methods 18 (2) (2021) 203–211, http://dx.doi.org/10.1038/s41592-020-01008-z.

[46] A.S. Jassar, C.J. Brinster, M. Vergnat, J.D. Robb, T.J. Eperjesi, A.M. Pouch, A.T. Cheung, S.J. Weiss, M.A. Acker, J.H. Gorman III, R.C. Gorman, B.M. Jackson, Quantitative mitral valve modeling using real-time three-dimensional echocardiography: technique and repeatability, Ann. Thorac. Surg. 91 (1) (2011) 165–171, http://dx.doi.org/10.1016/j.athoracsur.2010.10.034, URL https://www.annalsthoracicsurgery.org/article/S0003-4975(10)02379-9/pdf, 1552-6259 Jassar, Arminder Singh Brinster, Clayton J Vergnat, Mathieu Robb, J Daniel Eperjesi, Thomas J Pouch, Alison M Cheung, Albert T Weiss, Stuart J Acker, Michael A Gorman, Joseph H 3rd Gorman, Robert C Jackson, Benjamin M R01 HL073021-05A2/HL/NHLBI NIH HHS/United States R01 HL073021/HL/NHLBI NIH HHS/United States R01 HL103723/HL/NHLBI NIH HHS/United States HL73021/HL/NHLBI NIH HHS/United States R01 HL063954/HL/NHLBI NIH HHS/United States R01 HL063954-10/HL/NHLBI NIH HHS/United States HL63954/HL/NHLBI NIH HHS/United States Journal Article Research Support, N.I.H., Extramural Research Support, Non-U.S. Gov't Netherlands 2010/12/22 Ann Thorac Surg. 2011 Jan;91(1):165-71. doi: 10.1016/j.athoracsur.2010.10.034.

[47] L. Walczak, L. Tautz, M. Neugebauer, J. Georgii, I. Wamala, S. Sündermann, V. Falk, A. Hennemuth, Interactive editing of virtual chordae tendineae for the simulation of the mitral valve in a decision support system, Int. J. Comput. Assist. Radiol. Surg. 16 (1) (2021) 125–132, http://dx.doi.org/10.1007/s11548-020-02230-y, https://www.ncbi.nlm.nih.gov/pmc/articles/PMC7822807/pdf/11548_2020_Article_2230.pdf.

[48] P. Eulzer, S. Engelhardt, N. Lichtenberg, R. de Simone, K. Lawonn, Temporal views of flattened mitral valve geometries, IEEE Trans. Vis. Comput. Graphics 26 (1) (2020) 971–980, http://dx.doi.org/10.1109/tvcg.2019.2934337, URL https://ieeexplore.ieee.org/document/8805441/, 1941-0506 Eulzer, Pepe Engelhardt, Sandy Lichtenberg, Nils de Simone, Raffaele Lawonn, Kai Journal Article Research Support, Non-U.S. Gov't United States 2019/08/20 IEEE Trans Vis Comput Graph. 2020 Jan;26(1):971-980. doi: 10.1109/TVCG.2019.2934337. Epub 2019 Aug 19.